The Astrophysical Journal, 766:17 (14pp), 2013 March 20 doi:10.1088/0004-637X/766/1/17

TESTING FOR AZIMUTHAL ABUNDANCE GRADIENTS IN M101

Yanxia Li[1], Fabio Bresolin[1], and Robert C. Kennicutt, Jr.[2]
[1] Institute for Astronomy, 2680 Woodlawn Dr., Honolulu, HI 96822, USA
[2] Institute of Astronomy, University of Cambridge, Madingley Road, Cambridge CB3 0HA, UK
Received 2012 November 7; accepted 2013 January 31; published 2013 March 1

ABSTRACT

New optical spectra of 28 H II regions in the M101 disk have been obtained, yielding 10 new detections of the [O III] λ4363 auroral line. The oxygen abundance gradient measured from these data, combined with previous observations, displays a local scatter of 0.15 ± 0.03 dex along an arc in the west side of the galaxy, compared with a smaller scatter of 0.08 ± 0.01 dex in the rest of the disk. One of the H II regions in our sample (H27) has a significantly lower oxygen abundance than surrounding nebulae at a similar galactocentric distance, while an additional, relatively nearby one (H128) was already known to have a high oxygen abundance for its position in the galaxy. These results represent marginal evidence for the existence of moderate deviations from chemical abundance homogeneity in the interstellar medium of M101. Using a variety of strong-line abundance indicators, we find no evidence for significant large-scale azimuthal variations of the oxygen abundance across the whole disk of the galaxy.

Key words: galaxies: abundances – galaxies: individual (M101) – galaxies: ISM – ISM: abundances

Online-only material: color figures

1. INTRODUCTION

Radial gradients of metallicity in spiral galaxies have been known for a long time, with typical values of 0.03–0.10 dex kpc^{-1}. The study of giant extragalactic H II regions offered the first evidence for the presence of oxygen abundance gradients in galaxies (Searle 1971) and has been extensively used to probe the stellar populations and the chemical composition of nearby star-forming galaxies (Vila-Costas & Edmunds 1992; Zaritsky et al. 1994; van Zee et al. 1998; Bresolin et al. 1999), placing strong constraints on galactic chemical evolution models (Chiappini et al. 2001; Fu et al. 2009). In contrast, surprisingly little is known about the possible presence of azimuthal asymmetries in the abundance distribution in spiral disks. From a theoretical point of view, a virtually uniform distribution with negligible scatter could be expected along the azimuthal direction as a result of relatively fast mixing processes (except near corotation; Scarano & Lépine 2013) with timescales on the order of ∼100 Myr, in the turbulent interstellar medium (Roy & Kunth 1995; Yang & Krumholz 2012).

Deviations of the *radial* abundance gradient from a simple exponential seem to be well-established from studies of Cepheids (e.g., Luck et al. 2003) and open clusters (Twarog et al. 1997; Lépine et al. 2011), showing a discontinuity at a galactocentric distance of ∼8.5 kpc and a flattening beyond that radius, possibly caused by the barrier effect of corotation, which isolates the inner and outer regions of the disk one from the other due to opposite directions of gas flow (Lépine et al. 2011). Similar features can be observed in the H II region abundance distribution of nearby spiral galaxies (Bresolin et al. 2009b, 2012; Scarano et al. 2011). Investigations of Cepheids (Pedicelli et al. 2009) and H II regions (Balser et al. 2011) in the Milky Way have provided indications for the presence, at least near the corotation radius, of *azimuthal* gradients (∼0.05 dex kpc^{-1}) and chemical inhomogeneities, which can be attributed to the spiral arm structure and the consequent non-uniformity of the spatial distribution of gas and star formation in the disk of the Galaxy (Lépine et al. 2011). These results stress the importance of including the azimuthal coordinate, in addition to the radial one, in modeling the chemical evolution of the Milky Way.

The situation in other spiral galaxies is less clear, and suffers from poor statistics (small number of H II regions studied in a given galaxy) and measurement uncertainties. In the galaxy M33, Rosolowsky & Simon (2008) measured a substantial intrinsic dispersion of 0.11 dex (in addition to the dispersion due to observing errors) in the H II region oxygen abundance at constant radius. However, Bresolin (2011) showed that this is due to poor detections of the [O III] λ4363 auroral line used to derive nebular electron temperatures, and that a much smaller scatter of ∼0.06 dex, consistent with the measurement uncertainties, is obtained from the best-quality data. In a wide-field integral field spectroscopy study of NGC 628, Rosales-Ortega et al. (2011) found that the radial metallicity gradient varies slightly for different quadrants, although the differences are comparable to the uncertainties introduced by the nebular abundance diagnostics and can be related instead to systematic variations of the ionization parameter. The narrow-band imaging across the disk of the same galaxy by Cedrés et al. (2012) suggests that the detection of chemical inhomogeneities may depend on the choice of strong-line diagnostics used to derive the oxygen abundances. Recently, a large degree of inhomogeneity on relatively small spatial scales (∼0.5 kpc) has been claimed by Sanders et al. (2012) for the H II region oxygen abundances in M31. This result is not confirmed by other investigations in the same galaxy, including the recent one by Zurita & Bresolin (2012), and it is in general still unclear what role the sample selection and choice of chemical abundance diagnostics play in these results.

In an attempt to provide new observational constraints on the presence of chemical inhomogeneities and azimuthal gradients in nearby spiral galaxies, we turned to M101 (NGC 5457), a nearby (D = 6.85 Mpc; Freedman et al. 2001), nearly face-on, grand-design spiral galaxy that has been widely studied as a prototype system for the investigation of radial gradients of element abundances (see Kennicutt et al. 2003 and Bresolin 2007 for a review and references). There are more

than 10^3 cataloged H II regions in its disk (Hodge et al. 1990). Kennicutt & Garnett (1996) suggested the presence of a possible azimuthal asymmetry in the oxygen abundance distribution between the southeast (SE) and northwest (NW) regions of M101, based on strong-line abundance diagnostics. However, this result is subject to the uncertainties and discrepancies concerning the calibrations of these diagnostics (Bresolin 2007; Kewley & Ellison 2008). Kennicutt et al. (2003) improved on previous studies using *direct* oxygen measurements for 20 H II regions, which rely on the determination of the electron temperature from auroral-to-nebular line ratios, such as [O III] λ4363/λ5007. These authors found a ∼0.2 dex metallicity spread for H II regions located at a similar galactocentric distance in the southwestern section of the galaxy. However, limited by the size of their H II region sample, they could not confirm the large-scale azimuthal asymmetry between the SE and NW suggested by Kennicutt & Garnett (1996).

In this paper, we present new spectroscopic observations of 28 H II regions in M101, and are able to derive direct oxygen abundances for a subset of 10. This new dataset allows us to address the possibility of a non-axisymmetric distribution of the nebular oxygen abundance in this galaxy. In addition, because M101 is known to be currently experiencing an infall of high-velocity gas, as shown by H I maps (Sancisi et al. 2008), and has likely been recently subjected to interaction events, as shown by the lopsidedness of its disk, the peculiar spiral structure and faint tidal structures (Waller et al. 1997; Mihos et al. 2012), it is well suited to verify to what extent these events can affect the distribution of metals in a spiral disk.

This paper is organized as follows. In Section 2 we describe the observations and data reduction procedures. In Section 3 we present and analyze the radial gradients, and the local azimuthal variations of oxygen abundance, using both the direct method ([O III] λ4363-based) and strong-line diagnostics. We test the asymmetry of the oxygen abundance distribution between the east and west sections of M101 in Section 4, and present our conclusions in Section 5.

2. OBSERVATIONS

We obtained multi-object spectroscopy of M101 during the nights of 2010 May 7–8 with the R-C spectrograph at the Mayall 4-m telescope of the Kitt Peak National Observatory, using multi-object masks in five different fields, with 2 arcsec-wide slits. The data were acquired at airmasses smaller than 1.25 to minimize the impact of differential atmospheric dispersion. In each field we integrated for 3 × 2400 s using the KPC-10A grating (2.75 Å pixel^{-1}), which yielded a ∼7.5 Å FWHM spectral resolution and covering approximately the wavelength range between 3600 Å and 7500 Å.

Standard IRAF[3] tasks, in combination with the PyRAF[4] command language, were used for bias subtraction, flat-field correction, cosmic ray removal, spectral extraction, image co-addition, and wavelength calibration (using He+Ne+Ar lamp frames). We extracted one-dimensional spectra for each target H II region after executing all the standard reduction procedures. Three standard stars (Feige 34, Feige 67, and BD+28 4211) were observed several times each night for the flux calibration.

[3] IRAF is distributed by the National Optical Astronomy Observatory, which is operated by the Association of Universities for Research in Astronomy, Inc., under cooperative agreement with the National Science Foundation.

[4] PyRAF is a product of the Space Telescope Science Institute, which is operated by AURA for NASA.

Table 1
Observed H II Region Sample

ID[a]	R.A.[b] (J2000.0)	Decl.[c] (J2000.0)	R/R_0[d]	ϕ[e] (degree)	Other ID[f]
1	14 02 46.92	54 14 50.1	0.50	212	H219
2	14 02 53.68	54 15 22.8	0.43	206	H321
3	14 02 57.54	54 15 59.8	0.37	204	H370
4	14 02 30.61	54 16 09.7	0.54	232	H149
5	14 02 25.73	54 17 34.2	0.53	244	H103
6	14 02 49.83	54 17 43.0	0.32	226	H260
7	14 02 48.78	54 17 56.3	0.32	229	H237
8	14 02 18.22	54 18 36.6	0.58	254	H41
9	14 02 27.01	54 19 33.0	0.48	258	H120
10	14 02 29.49	54 19 47.7	0.45	260	H140
11	14 02 19.92	54 19 57.1	0.55	263	H59
12	14 02 16.85	54 21 00.1	0.58	271	H27
13	14 02 22.06	54 21 57.7	0.54	278	H79
14	14 02 17.83	54 22 32.4	0.59	282	H37[g]
15	14 02 17.83	54 22 32.4	0.59	282	H37[g]
16	14 02 20.39	54 23 13.7	0.58	287	H68
17	14 02 27.50	54 27 08.0	0.66	313	H125
18	14 03 50.86	54 27 35.9	0.61	40	H1151
19	14 03 49.98	54 27 50.5	0.61	38	H1148[g]
20	14 03 49.98	54 27 50.5	0.61	38	H1148[g]
21	14 03 49.18	54 28 10.0	0.63	36	H1146
22	14 04 49.80	54 28 14.0	1.12	63	H1262
23	14 03 46.84	54 28 37.3	0.64	33	H1137
24	14 02 39.30	54 29 04.9	0.69	329	H188
25	14 02 49.65	54 29 07.0	0.64	338	H253
26	14 03 44.30	54 29 14.4	0.66	29	H1121
27	14 03 43.26	54 29 49.4	0.69	27	H1118
28	14 03 13.70	54 35 47.0	1.05	1	H681

Notes.
[a] H II region identification (in order of increasing declination).
[b] Right ascension. Units are hours, minutes, and seconds.
[c] Declination. Units are degrees, arcminutes, and arcseconds.
[d] Deprojected galactocentric distance in units of the isophotal radius, $R_0 = 14.'4$, taken from de Vaucouleurs et al. (1991).
[e] Position angle relative to the galaxy center, in degrees.
[f] Identification from Hodge et al. (1990).
[g] Two objects in the same slit.

Our observations yielded spectra for 28 H II regions. Their celestial coordinates, galactocentric distances normalized to the isophotal radius R_0, position angles ϕ relative to the galactic center, and identifications from the Hodge et al. (1990) catalog are presented in Table 1 (where objects are listed in order of increasing declination). We have adopted the following parameters: center coordinates R.A. = 14:03:12.5, Decl. = +54:20:56 (J2000), position angle of the major axis = 37 deg, inclination angle = 18 deg (de Blok et al. 2008), distance = 6.85 Mpc (Freedman et al. 2001), and isophotal radius $R_0 = 14.'4$ (de Vaucouleurs et al. 1991), corresponding to 28.7 kpc. Figure 1 shows the location of the target H II regions in M101. H II regions for which we detected the [O III] λ4363 auroral line are labeled by double symbols, and we identify the different data sources considered in this paper with different symbols.

2.1. Line Flux Measurement

The emission line intensities were measured with the *splot* routine in IRAF by integrating the flux under the line profiles between two continuum points selected interactively. A multi-Gaussian profile fit was performed if evident line blending occurred. A correction for interstellar reddening was performed

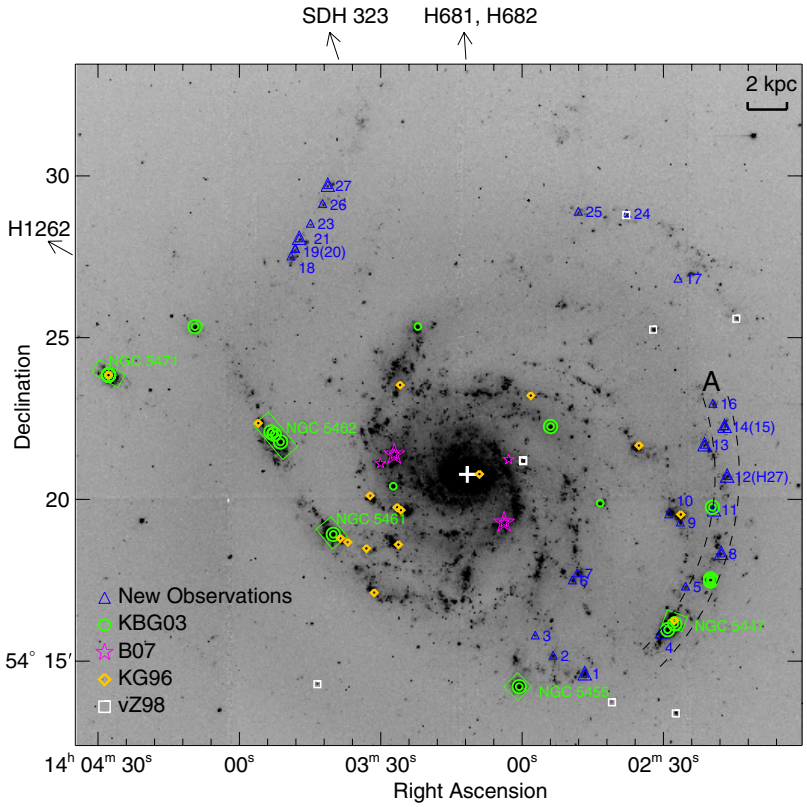

Figure 1. Location of the H II regions in our study on a narrow-band Hα image of M101 (from the Canada–France–Hawaii Telescope data archive). The white cross marks the center of the galaxy. The symbols indicate the different data sources: blue triangles—new observations; green circles—Kennicutt et al. (2003); magenta stars—Bresolin (2007); orange diamonds—Kennicutt & Garnett (1996); white squares—van Zee et al. (1998). H II regions with [O III] λ4363 detections are labeled by doubled line symbols. Note that four distant objects (H1262, H681, H682, and SDH323) are outside the field of view (the arrows indicate the directions to these nebulae). The two curved dashed lines in the west mark the position of "arc A."

(A color version of this figure is available in the online journal.)

adopting the Howarth (1983) analytical formulation of the Seaton (1979) law, assuming a total-to-selective extinction ratio $R_V = A_V/E_{B-V} = 3.1$. By comparing the measured intensities of Hα and Hγ, relative to Hβ, to the case B theoretical values taken from Storey & Hummer (1995) calculated at the electron temperatures determined from the auroral lines (or 10,000 K if these lines were not detected), we obtained the reddening coefficient c(Hβ). The Balmer lines ratios (Hα/Hβ, Hγ/Hβ) were corrected for underlying stellar absorption in an iterative manner. The resulting reddening-corrected line flux measurements, normalized to Hβ = 100, are tabulated in Table 2. The errors in these fluxes were estimated from the uncertainties in the line intensity measurements and the flux calibration, the scatter of the continuum near the emission lines, and the uncertainties in the extinction coefficient. We note that, in general, the H II regions in our sample are extended and are not fully covered by the width of our slits. Thus, the Hβ fluxes reported in Table 2 should be considered lower limits to the real fluxes.

2.2. Electron Temperatures and Oxygen Abundances

Electron temperatures and oxygen abundances were obtained adopting a two excitation zone structure for the H II regions characterized by the temperatures T[O II] and T[O III]. To calculate the total oxygen abundances, we made the usual assumption:

$$\mathrm{O/H} = (\mathrm{O^+} + \mathrm{O^{++}})/\mathrm{H^+}. \quad (1)$$

The electron temperature (T_e) for the O^{++}-emitting region (T[O III]) and for the O^+-emitting region (T[O II]) were derived from the auroral-to-nebular line intensity ratios ([O III] λ4363/$\lambda\lambda$4959, 5007 and [O II] λ7325/λ3727), when available, with the *nebular* module (Shaw & Dufour 1995) of the STSDAS package running under IRAF. For nebulae without auroral line detections we adopted $T_e = 10^4$ K. One or both of the [O III] λ4363 and [O II] λ7325 auroral lines could be measured in 10 out of the 28 H II regions in our sample: 7 objects with both lines detected, 3 with only [O III] λ4363 detected, and 1 with only [O II] λ7325 detected. We compared our measured T[O II] values with those obtained from the theoretical relation obtained by Garnett (1992):

$$T[\mathrm{O\,II}] = 0.70T[\mathrm{O\,III}] + 3000\ \mathrm{K} \quad (2)$$

and found that the two were consistent with each other within the uncertainties. However, since the T[O II] values obtained from the auroral-to-nebular line ratios have significantly larger errors (between 300 K and 900 K) than those propagated from T[O III] through Equation (2) (170 K to 400 K), a result already noted by Kennicutt et al. (2003), we decided to adopt the T[O II] values calculated via Equation (2). In the end, this choice has a limited impact on the abundance determination since the O/H ratios obtained by adopting one or the other set of T[O II] values differ only by a few hundreds of a dex (0.07 dex at most), except for H59, where the difference is 0.13 dex.

Table 2
Dereddened Line Fluxes, Temperatures, and Oxygen Abundances from the Direct Method

ID	Name	[O II] λ3727	[O III] λ4363	[O III] λ5007	[N II] λ6583	[S II] λλ6717,6731	$F(H\beta)$ (erg s^{-1} cm^{-2})	$c(H\beta)$ (mag)	T [O III] (K)	12 + log(O/H)
1	H219	413 ± 21	0.91 ± 0.05	178 ± 8	36.0 ± 1.5	41.3 ± 1.3	3.8×10^{-14}	0.31	9420 ± 258	8.42 ± 0.08
2	H321	264 ± 13	...	237 ± 11	29.5 ± 1.2	24.7 ± 0.7	3.3×10^{-14}	0.43	...	...
3	H370	283 ± 14	...	129 ± 6	78.3 ± 2.8	54.4 ± 1.4	1.6×10^{-14}	0.53	...	...
4	H149	238 ± 12	1.68 ± 0.08	329 ± 15	35.6 ± 1.5	39.4 ± 1.2	1.6×10^{-13}	0.35	9411 ± 247	8.40 ± 0.08
5	H103	343 ± 17	...	158 ± 7	42.6 ± 2.0	38.6 ± 1.3	1.3×10^{-14}	0.18	...	...
6	H260	245 ± 12	...	207 ± 9	36.6 ± 1.4	35.4 ± 1.0	3.6×10^{-14}	0.45	...	...
7	H237	193 ± 10	...	106 ± 5	47.5 ± 1.7	38.5 ± 1.0	8.2×10^{-14}	0.51	...	...
8	H41	169 ± 9	3.92 ± 0.18	476 ± 21	8.4 ± 0.4	15.8 ± 0.5	3.7×10^{-14}	0.28	10894 ± 327	8.25 ± 0.08
9	H120	419 ± 21	...	82 ± 4	63.3 ± 2.8	86.9 ± 2.8	1.9×10^{-14}	0.26	...	...
10	H140	352 ± 18	...	145 ± 7	57.0 ± 2.5	67.1 ± 2.1	3.1×10^{-14}	0.29	...	...
11	H59	305 ± 15	2.30 ± 0.11	290 ± 13	17.2 ± 0.8	25.9 ± 0.9	2.1×10^{-14}	0.16	10769 ± 322	8.24 ± 0.08
12	H27	341 ± 17	3.64 ± 0.17	251 ± 11	21.6 ± 1.0	58.0 ± 2.0	2.1×10^{-14}	0.16	13401 ± 499	7.96 ± 0.08
13	H79	226 ± 11	3.04 ± 0.15	330 ± 15	15.5 ± 0.7	27.1 ± 0.9	1.7×10^{-14}	0.25	11313 ± 563	8.14 ± 0.11
14	H37	236 ± 12	...	333 ± 15	19.2 ± 0.9	22.1 ± 0.8	8.6×10^{-15}	0.19	...	...
15	H37	234 ± 12	3.31 ± 0.16	387 ± 17	14.9 ± 0.6	28.5 ± 0.8	2.5×10^{-14}	0.38	11043 ± 344	8.22 ± 0.08
16	H68	391 ± 19	...	171 ± 7	33.8 ± 1.5	75.6 ± 2.5	1.1×10^{-14}	0.26	...	...
17	H125	350 ± 18	...	327 ± 15	29.0 ± 1.4	33.3 ± 1.3	1.3×10^{-15}	0.15	...	...
18	H1151	397 ± 21	...	158 ± 7	25.0 ± 1.0	35.4 ± 1.1	2.1×10^{-15}	0.43	...	...
19	H1148	177 ± 9	...	293 ± 13	17.5 ± 0.8	25.6 ± 0.8	7.9×10^{-15}	0.28	...	...
20	H1148	199 ± 10	...	383 ± 17	11.0 ± 0.4	14.5 ± 0.4	1.5×10^{-14}	0.40	...	...
21	H1146	212 ± 11	3.07 ± 0.15	457 ± 20	17.7 ± 0.8	27.1 ± 0.9	9.6×10^{-15}	0.27	10219 ± 299	8.35 ± 0.08
22	H1262	200 ± 10	...	316 ± 14	13.0 ± 0.7	31.6 ± 1.1	3.4×10^{-15}	0.22	...	...
23	H1137	378 ± 19	...	25 ± 1	43.7 ± 2.0	87.5 ± 2.9	2.3×10^{-15}	0.25	...	...
24	H188	682 ± 34	...	164 ± 7	23.8 ± 1.1	58.7 ± 2.0	3.9×10^{-15}	0.23	...	...
25	H253	430 ± 22	...	73 ± 3	40.8 ± 1.9	84.6 ± 2.9	3.6×10^{-15}	0.17	...	...
26	H1121	336 ± 17	...	217 ± 10	29.3 ± 1.3	47.7 ± 1.6	5.7×10^{-15}	0.26	...	...
27	H1118	222 ± 11	5.97 ± 0.29	559 ± 25	8.9 ± 0.4	11.4 ± 0.4	6.4×10^{-15}	0.27	11917 ± 402	8.21 ± 0.08
28	H681	232 ± 12	4.36 ± 0.20	260 ± 12	9.7 ± 0.3	27.7 ± 0.7	2.6×10^{-14}	0.59	14237 ± 559	7.80 ± 0.09

Notes. Line fluxes are normalized to $H\beta = 100$, after correcting for reddening. F($H\beta$) is the measured $H\beta$ flux, corrected for extinction.

The measured T_e values of the O^{++}-emitting region are presented in Table 2. We assume, as indicated by the [S II] λ6717/ λ6731 line ratios, that all H II regions are in the low density limit ($n_e < 10^2$ cm^{-3}).

We derived the oxygen abundances both from the measurement of the electron temperature ("direct" method or T_e method), obtained as explained above, and strong-line diagnostics. Strong-line diagnostics were put forward to obtain the abundances in H II regions when the temperature-sensitive lines are not accessible (e.g., in metal-rich regions or high redshift galaxies), by using combinations of more easily measured strong emission lines as indicators of the abundance, such as the popular [O II] λ3727 + [O III] λλ4959, 5007)/$H\beta$ line ratio, otherwise known as R_{23} (Pagel et al. 1979). As is well known, strong-line indicators like R_{23} can suffer from degeneracy when calculating the chemical abundances, and abundances derived from different strong-line methods and/or calibrations can vary systematically up to $\Delta\log(O/H) = 0.7$ dex (Kewley & Ellison 2008).

2.3. The Enlarged Sample

In order to increase the sample size and to cover a larger radial and azimuthal range, we also collected data from additional sources:

1. Kennicutt & Garnett (1996, KG96) presented spectroscopic data for 41 H II regions, including some distinct knots in large complexes (NGC 5462, NGC 5447, and NGC 5471), which could be used as control samples to examine the intrinsic metallicity variation if we assume that within their volume the oxygen abundance is homogeneous.
2. Kennicutt et al. (2003, KBG03) observed 26 H II regions, with 23 targets in common with KG96; 17 of those 23 observations yielded [O III] λ4363 measurements. In addition, they also observed three new objects: H70, H71, and SDH323 (following the designation in KBG03), all of them with [O III] λ4363 measurements.
3. Bresolin (2007, B07) observed four H II regions (H1013, H493, H507, and H972) in the inner (central 3′), metal-rich zone of M101; two (H1013 and H493) provided reliable T_e measurements.
4. van Zee et al. (1998, vZ98) published spectroscopic data for 13 H II regions in M101. These authors did not follow the object identification from the catalog of Hodge et al. (1990). Based on their map of slit positions, we identified the corresponding objects in Hodge et al. (1990).

In assembling our catalog of line fluxes for H II regions in M101, we adopted the more accurate line fluxes given by KBG03 and B07 for the 26 objects in common with KG96. Similarly, for H67 and H188, which were observed by vZ98, we adopted our new data or those by KBG03. Since in KG96 and vZ98 only the sum of the [O III] λλ4959, 5007 and [N II] λλ6548,6583 line fluxes are given, we calculated the individual line fluxes of the lines in the doublets using the theoretical ratios (Storey & Zeippen 2000).

Table 3 presents line fluxes from different authors (KBG03 and B07) for the six objects in common with our new dataset of 28 H II regions (labeled as "New" in the table). In Figure 2

Table 3
Comparison with Previous Observations

		H1013[a]	H972[a]	H237[b]	H149[b]	H140[b]	H681[b]
	KBG03	188	148	136	212	317	244
[O II] λ3727	B07	221	139	...	...	...	...
	New	...	...	192.8	238.5	351.8	232
	KBG03	103	30	114	318	114	304
[O III] λ5007	B07	102	30	...	...	...	...
	New	...	...	106.1	328.6	145.4	259
	KBG03	64.6	86.9	48.3	35.9	60.2	11.3
[N II] λ6583	B07	71	80	...	...	...	...
	New	...	...	47.5	35.6	57	9.7
	KBG03	28.8	38.4	35.3	37.2	80.9	27
[S II] λλ6717,6731	B07	29.8	41	...	...	...	...
	New	...	...	38.5	39.4	67.1	27.7
	KBG03	...	...	...	1.8	...	...
[O III] λ4363	B07	0.24	...	...	...	...	...
	New	...	...	...	1.7	...	...
R_{23}	KBG03	3.27	1.88	2.90	6.40	4.71	6.54
	B07	3.58	1.79	...	...	...	...
	New	...	...	3.36	6.81	5.48	5.82
$12 + \log(O/H)_{T_e}$	KBG03	8.71	...	...	8.33	...	7.92
	B07	8.52	...	...	...	...	...
	New	...	...	...	8.40	...	7.80

Notes. Six H II regions are in common between KBG03, B07, and our new observations.
[a] For H1013 and H972, the B07 line fluxes were adopted to construct the enlarged H II region sample (see the text).
[b] For H237, H149, H140, and H681 the newly-determined line fluxes from our observations were used for the enlarged sample.

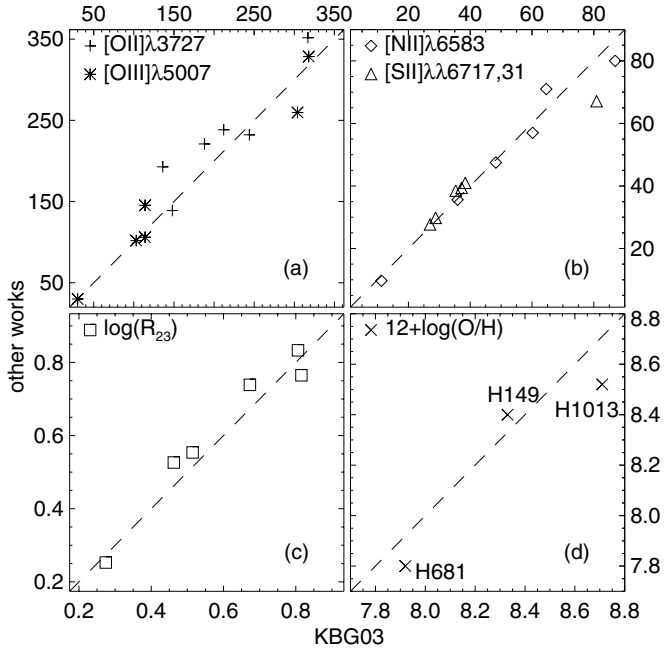

Figure 2. Comparison of line fluxes and derived quantities for H II regions from our new observations and those by Kennicutt et al. (2003; KBG03). (a) [O II] λ3727 (crosses) and [O III] λ5007 (asterisks); (b) [N II] λ6583 (diamonds) and [S II] λλ6717, 6731 (triangles); (c) $\log(R_{23})$; (d) T_e-based oxygen abundances. The dashed line represents the one-to-one correlation.

we display a comparison of line fluxes and derived quantities (R_{23}, O/H).

The agreement between the different studies is generally satisfactory. There is only one object, H140, with a considerable difference (∼20%) in the [S II] flux between our new observations and those by KBG03. Figure 2(c) indicates that R_{23} values are consistent between the different studies, with differences <0.12 dex. There are only three objects in common that also have an [O III]-λ4363-based oxygen abundances. For H1013, B07 provided an oxygen abundance 0.21 dex lower than KBG03. We adopted the value from B07, obtained from deeper data, and which corresponds to an O^{++} zone temperature directly derived from [O III] λ4363/(λ4959 + λ5007), while in KBG03 it was derived from T [S III]. Finally, we adopted the H972 measurements from B07, while for the remaining four H II regions included in Table 3 our new observations were adopted.

Our final sample comprises 79 H II regions, with 28 objects from our new observations, 20 from KBG03, 4 from B07, 16 from KG96 and 11 from vZ98. In this merged sample, there are 29 measurements of the [O III] λ4363 auroral line (10 from our new observations, 17 from KBG03 and 2 from B07). In order to ensure consistency in the analysis, we recalculated the T_e and the direct oxygen abundances when the [O III] λ4363 line was measured.

In Figure 3 we examine the excitation properties of our H II region sample by plotting the classic [O III] λ5007/Hβ versus [N II] λ6583/Hα and [O III] λ5007/Hβ versus [S II] λ6717, 6731/Hα diagnostic diagrams (Baldwin et al. 1981, BPT).

We include in the plot the boundaries between different photoionization sources (star-forming regions versus active galactic nuclei) by Kewley et al. (2001; shown by the long-dashed line) and (Kauffmann et al. 2003; short-dashed line). Kewley et al. (2001) used stellar population synthesis and photoionization models to create the "maximum starburst line" on the BPT diagrams. A modification to this classification was provided

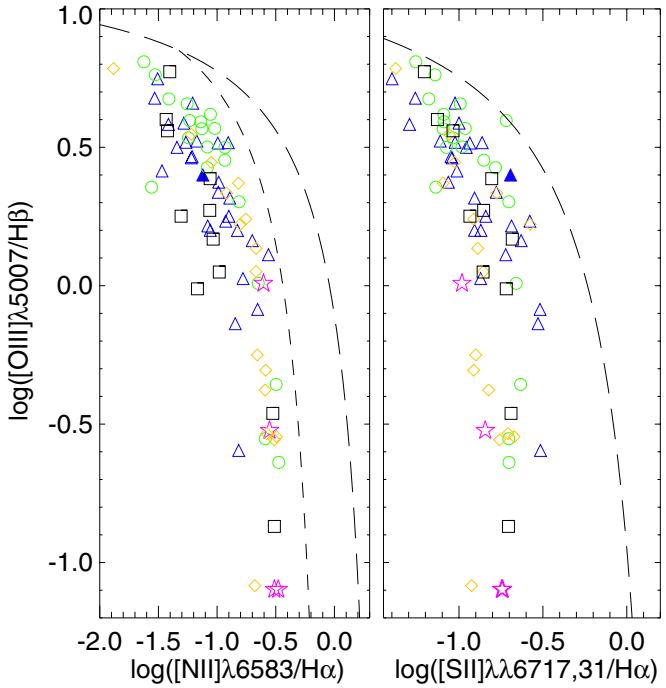

Figure 3. Nebular diagnostic diagrams showing the excitation sequence for our H II region sample: log([N II] λ6583/Hα) (left) and log([S II] λλ6717, 6731/Hα) (right) as a function of log([O III] λ5007/Hβ). The curves represent upper boundaries for star-forming regions ionized by hot stars from Kewley et al. (2001; long-dashed line) and Kauffmann et al. (2003; short-dashed line). The filled blue triangles mark the positions of H27 in our new observations. Symbols as in Figure 1.

(A color version of this figure is available in the online journal.)

by Kauffmann et al. (2003) to include an empirical boundary line between pure star-forming galaxies and Seyfert-H II composite objects. As shown in Figure 3, according to these criteria all the objects in our sample are located in the pure star-forming region of the diagram.

3. RADIAL ABUNDANCE GRADIENT AND LOCAL AZIMUTHAL VARIATIONS

The first measurements of a radial abundance gradient from H II regions in M101 can be traced back to more than 40 years ago (Searle 1971; Smith 1975). Based on our new spectroscopic observations, in combination with the work published by other authors as presented in Section 2, we are in the position to better assess the spatial distribution of the oxygen abundance in the disk of this galaxy. Given the relatively dense spectroscopic coverage in the western part of the disk, we can investigate how the oxygen abundance varies along the arc-like region identified in Figure 1, designated as *arc A* hereafter, covering the restricted radial range $R/R_0 = 0.54$ to 0.59 and extending in position angle between 230 and 290 deg (∼17 kpc in projected length), where we have a good amount of nebular spectra with [O III] λ4363 detections, in order to test whether we could confirm the local azimuthal variation suggested by KG96.

3.1. Abundance Variations Based on the Direct Method

There are 29 H II regions with [O III] λ4363 line measurements in our sample, covering the radial range from $R/R_0 = 0.10$ (H493) to $R/R_0 = 1.25$ (SDH323). The resulting radial oxygen abundance gradient is presented in Figure 4. As the figure shows, the data can be well fitted by a weighted linear least-squares fit (the linear Pearson correlation coefficient is −0.90):

$$12 + \log(\mathrm{O/H})_{T_e} = 8.73(\pm0.03) - 0.87(\pm0.04) R/R_0, \quad (3)$$

which, unsurprisingly, is consistent with previous results by KBG03, $12 + \log(\mathrm{O/H})_{T_e} = 8.76(\pm0.06) - 0.90(\pm0.08) R/R_0$, and B07, $12 + \log(\mathrm{O/H})_{T_e} = 8.75(\pm0.05) - 0.90(\pm0.07) R/R_0$.

Let us examine the abundance distribution along arc A. As shown by the gray shadowed region in Figure 4, this part of the galaxy contains objects whose O/H abundance ratios appear to cover a larger spread (at constant radius) than elsewhere. To clarify the situation, in Figure 5 we zoom into this restricted radial range (top panel), and plot the oxygen abundance as a function of position angle (bottom panel). The red dotted lines mark the range in O/H corresponding to the change in galactocentric distance from 0.54 R_0 to 0.59 R_0, as inferred from the gradient given by Equation (3).

The H II region H27 stands out with an abundance 12 + log(O/H) = 7.96 ± 0.08, while the corresponding radial fit value at its galactocentric distance is 8.23 ± 0.05. The difference between the measured and the fit value is 0.27 ± 0.09 dex. Therefore, H27 is a 3σ outlier from the linear fit. An additional object observed by KBG03, H128, is also an outlier relative to the radial fit with an observed value of 12 + log(O/H) = 8.45 ± 0.04 dex and a fit value of 8.25 ± 0.05 dex (∼3.1σ). All other objects are consistent with the radial fit value for their galactocentric distances within 3× their measurement uncertainties.

Like all other objects, H27 and H128 are located in the pure star-forming region of the BPT diagram (see Figure 3)

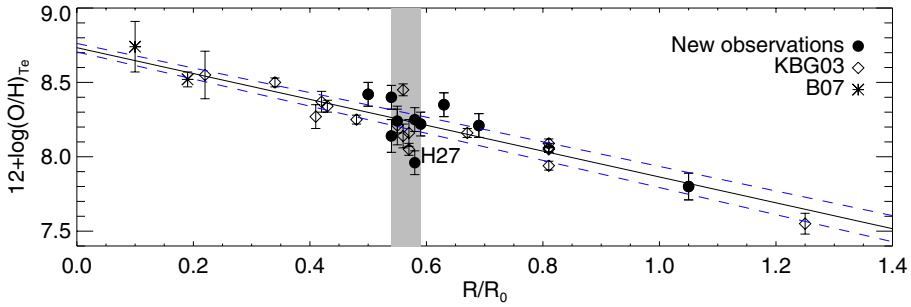

Figure 4. Radial oxygen abundance gradient determined from direct electron temperature measurements. The filled circles represent our new observations. The H II regions from KBG03 and B07 are labeled by the diamond and the asterisk symbols, respectively. The solid line is the weighted linear least-squares fit of all 29 H II regions in the figure, with the 1σ uncertainty represented by the two blue dashed lines. The grey shadowed region is the portion where we have the most data points in a radial range of ∼1.4 kpc ($R/R_0 = 0.54$ to 0.59). H27 is the H II region with the most significant oxygen abundance discrepancy relative to the linear fit.

(A color version of this figure is available in the online journal.)

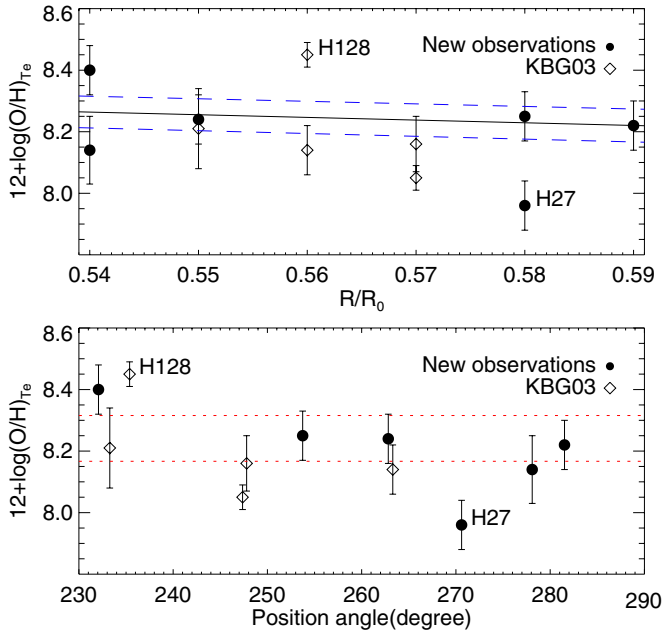

Figure 5. Enlargement of the gray shadowed region in Figure 4. The upper panel shows the relation between the oxygen abundance and the radial distance range $R/R_0 = 0.54$ to 0.59. The blue dashed line has the same meaning as in Figure 4. The bottom panel is the variation of the oxygen abundance with position angle. The region between the two red dotted lines is the maximum variation of the oxygen abundance due to the change of radial distance, calculated from Equation (3).

(A color version of this figure is available in the online journal.)

and we find no evidence for the presence of other ionization mechanisms (e.g., shocks) that could explain its peculiar oxygen abundance for its galactocentric distance. For example, we find no significant enhancement in the strength of shock-sensitive lines, such as [S II], [O I]. H27 lies within the region in which Franchetti et al. (2012) made a spatially-detailed investigation of supernova remnant (SNR) candidates in M101 from archival *Hubble Space Telescope* images, and has been identified as a superbubble, rather than an SNR.

Analyzing the scatter relative to the radial abundance gradient is one approach to probe azimuthal variations of metals (Bresolin 2011). The rms scatter around the least-squares fit for our full sample of H II regions (black solid line in Figure 4) is 0.11 dex. For the 11 objects contained within the grey shadowed portion such scatter rises to 0.15 dex, while for the 18 remaining objects it is 0.08 dex.

A scatter of 0.15 dex potentially represents a detection of local inhomogeneities in the abundance distribution. In order to test the significance of this result, we calculated the errors on the scatter measured for these two data sets (inside and outside the shadowed region in Figure 4), following a jackknife procedure (Lupton 1993, p. 46). Simply put, jackknife resamples a sample of size N, constructing N subsamples of size $N-1$ by omitting an element of the sample in succession, and then estimates the variance of the scatter t_N from

$$\sigma^2_{t_N} = \frac{N-1}{N}\sum_{i=1}^{N}(t_{N-1,i} - \bar{t}_{N-1})^2 \qquad (4)$$

where $\bar{t}_{N-1}$ is the average of t over the N subsamples.

By applying this technique, the resulting scatters are 0.15 ± 0.03 dex (objects within arc A) and 0.08 ± 0.01 dex (objects outside arc A), respectively. Thus, the significance of the difference is only at the $\sim 2\sigma$ level.

In summary, using the direct method on our enlarged sample of 29 H II regions with [O III] λ4363 detections, we derive a radial oxygen abundance gradient that is consistent with previous results. We detect two outliers from the mean radial gradient, H27 and H128, both of which with a significance at the 3σ level. No evidence of shocked gas are found for H27. The objects located along arc A display an abundance scatter of 0.15 ± 0.03 dex, which represents a marginal detection of a local azimuthal variation.

3.2. Abundance Variations Based on Strong-line Methods

3.2.1. Comparison of Different Strong-line Methods

In addition to the [O III] λ4363-based method, in order to take advantage of the 79 objects in our enlarged sample of H II regions we also considered a number of strong-line methods, in which the strength of easily observed nebular emission lines can be used to calculate the nebular abundances. Among the available methods making use primarily of O lines we considered the R_{23} calibration by McGaugh (1991, M91; in the analytical form provided by Kobulnicky et al. 1999), and the P-method by Pilyugin (2001, P01; 2005, P05). Other methods rely on the calibration of the strength of other emission lines, typically the N lines, in terms of the O abundance: Pettini & Pagel (2004; PP04-N2 and PP04-O3N2), Pérez-Montero & Contini (2009; PM09-N2 and PM09-O3N2), Pilyugin et al. (2010; ONS), Kewley & Dopita (2002, KD02), and the empirical calibration of [N II]/[O II] from Bresolin (2007; NO). These methods are summarized in Table 4 for clarity. They are somewhat arbitrarily divided in "empirically" and "theoretically" calibrated methods to reflect the fact that the calibration in terms of O/H abundance ratio can be obtained from samples of H II regions with available direct abundances or from grids of photoionization models, respectively.

For our purposes, we were interested to test how the strong-line abundances compared with the abundances from the direct method. We show in Figure 6 the comparison between H II region abundances obtained from the T_e method (along the x-axis) and those obtained from the various strong-line diagnostics. Since similar comparisons have appeared frequently in the literature in the past decade, presenting comparable results, we keep our discussion limited to the essential. For further details, the reader is referred to, for example: Kennicutt et al. (2003), Bresolin et al. (2009a), Kewley & Ellison (2008), Pérez-Montero & Díaz (2005), and Yin et al. (2007).

Empirically calibrated methods. The first two rows of Figure 6 refer to empirically calibrated diagnostics. A quick look at the figure shows that despite the fact that, by construction, these methods should generally agree with the direct method, the level of agreement varies greatly, at least for the sample of H II regions we are considering. In some cases this is due to the fact that the O/H range in which the diagnostics were calibrated is narrower than the full range of abundances available in M101 (which is unusually large). Secondly, possible differences in physical conditions (e.g., ionization parameter) between the calibrating sample and our sample can translate into the variations we observe. With these considerations in mind, we point out the following points:

1. PP04-N2 provides a relatively good match to the direct abundances (with a rms scatter of 0.11 dex), but large discrepancies arise at low metallicity, 12 +

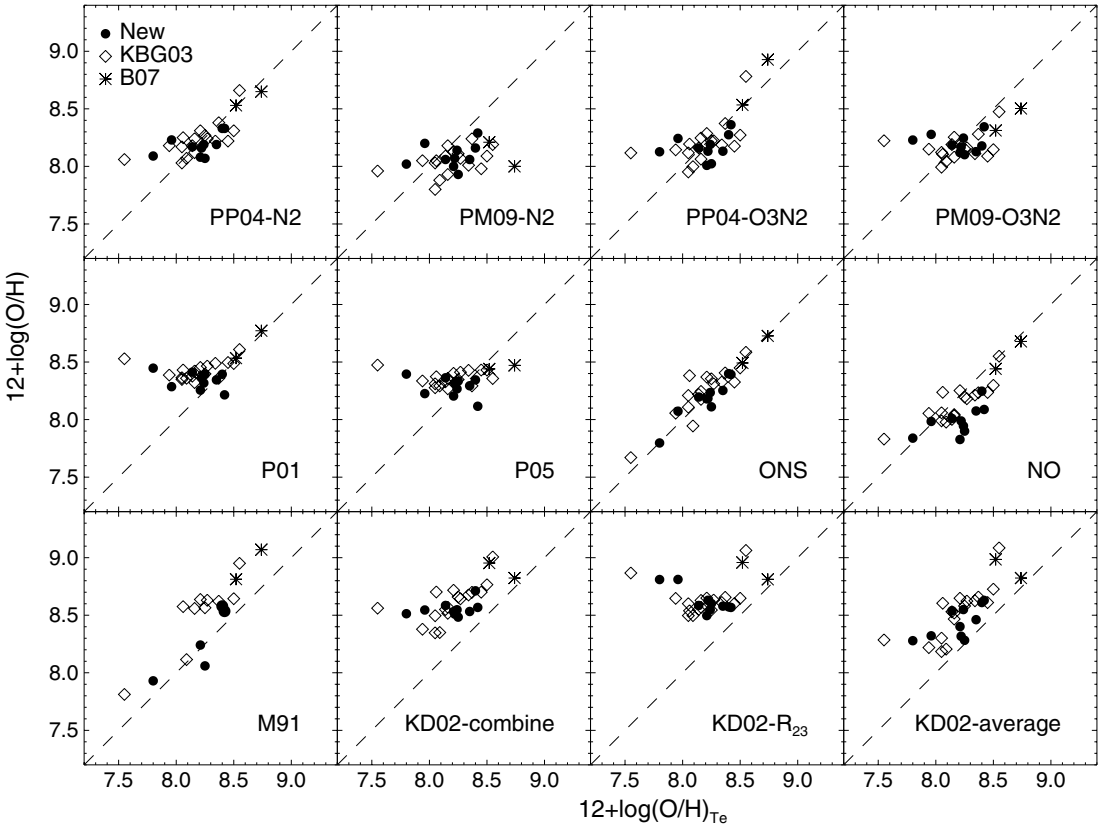

Figure 6. Comparison of oxygen abundances derived from different strong-line diagnostics with those obtained from the T_e method. For the M91 method only 17 objects with a well-established R_{23} branch attribution are plotted.

Table 4
Summary of Nebular Abundance Diagnostics Adopted

Number	Method	Emission Lines Involved	Calibration Class	References
1	T_e	[O III] λ4363, [O III] λ4959,5007	Direct	Aller (1984), Stasińska (2005)
2	PP04-N2	[N II]/Hα	Empirical	Pettini & Pagel (2004)
3	PM09-N2	[N II]/Hα, [N II]/[O II]	Empirical	Pérez-Montero & Contini (2009)
4	PP04-O3N2	[N II]/Hα, [O III]/Hβ	Empirical	Pettini & Pagel (2004)
5	PM09-O3N2	[N II]/Hα, [O III]/Hβ, [N II]/[O II]	Empirical	Pérez-Montero & Contini (2009)
6	P01[a]	R_{23}, [O III]/[O II]	Empirical	Pilyugin (2001)
7	P05[a]	R_{23}, [O III]/[O II]	Empirical	Pilyugin (2005)
8	ONS	[S II]/[O II], [N II]/[O II], [O III]/Hβ	Empirical	Pilyugin et al. (2010)
9	NO	[N II]/[O II]	Empirical	Bresolin (2007)
10	M91	R_{23}, [O III]/[O II]	Theoretical	McGaugh (1991), Kobulnicky et al. (1999)
11	KD02-combine[b]	[N II]/[O II], R_{23}, [O III]/[O II], [N II]/[S II]	Theoretical	Kewley & Dopita (2002)
12	KD02-R_{23}[c]	[N II]/[O II], R_{23}, [O III]/[O II]	Theoretical	Kewley & Dopita (2002)
13	KD02-average[d]	[N II]/[O II], R_{23}, [O III]/[O II]	Theoretical	Kewley & Dopita (2002)

Notes.
[a] $P \equiv$ [O III] λλ4959,5007/([O II] λ3727+ [O III] λλ4959,5007).
[b] Diagnostic recommended for an optimized abundance determination in KD02.
[c] The R_{23} method in KD02.
[d] The "combine average" method by KD02, which is the average of five independent strong-line methods.

log(O/H) < 8.0. Similarly for PP04-O3N2, but the scatter is worse (0.17 dex).

2. PM09-N2 tends to systematically underestimate the abundances, compared to the direct method. PM09-O3N2 yields similar results.
3. The P01 calibration was derived from nebular data with 12 + log(O/H) > 8.2, which is therefore the applicable range of this method. Accordingly, it is not surprising to see large discrepancies in the low metallicity regime.
4. P05 is a revised version of P01, providing calibrations for both the upper and the lower branch of the relation between oxygen abundance and R_{23}. Here, we only adopted the calibration for the upper branch, but even at high metallicity the diagnostic underestimates the T_e-based abundances.
5. The ONS calibration provides abundances that are comparable to those from the T_e method across the whole metallicity range, with a rms scatter of 0.09 dex.

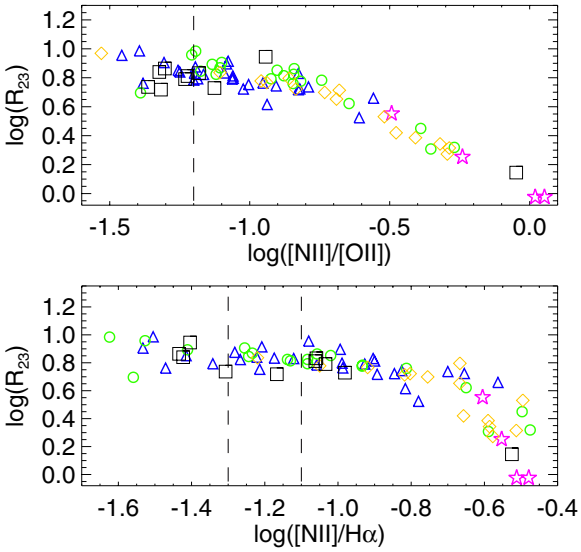

Figure 7. Top: observed relationship between the [N II] λ6583/[O II] λ3727 line ratio and the log(R_{23}) indicator. Bottom: observed relationship between the [N II] λ6583/Hα line ratio and the log(R_{23}) indicator. The dashed lines indicate the criteria to distinguish between the R_{23} upper and lower branches according to Kewley & Ellison (2008). Symbols as in Figure 1.

(A color version of this figure is available in the online journal.)

6. The NO calibration seems to largely agree with the T_e method, although the scatter of the data points is larger than in the case of the ONS method.

Theoretically calibrated methods. The last row of Figure 6 presents the abundances obtained from strong-line methods that are calibrated from theoretical models. It is well known that they provide systematically higher abundances than the T_e method (e.g., Bresolin et al. 2009a). "KD02-combine" represents the so-called "combined" diagnostic of KD02, recommended as an optimized abundance determination by these authors, and which can be used over the range of abundances from 12 + log(O/H) = 8.2 up to 9.4, with a minimized scatter and showing no systematic offset compared with "KD02-average." "KD02-R_{23}" is the R_{23} method calibrated from the models of KD02: compared to the T_e method it shows a large scatter both at high and low metallicities. "KD02-average" is the average of five independent strong-line methods. As we can see in Figure 6, it overestimates the T_e-based abundances, but the relative offset appears unchanged across the full metallicity range.

Finally, M91 suffers from the well-known double-valued nature of the R_{23} diagnostic. Additional line ratios and/or an initial guess of the abundance are required to choose the appropriate branch. We attempted to break the R_{23} degeneracy by using the [N II]/[O II] and [N II]/Hα ratios, following the criteria found in Kewley & Ellison (2008). According to these authors, the separation between the R_{23} upper and lower branches occurs at $\log([\mathrm{N\,II}]/[\mathrm{O\,II}]) = -1.2$ and $-1.3 \leqslant \log([\mathrm{N\,II}]/\mathrm{H}\alpha) \leqslant -1.1$. These boundary values are marked by dashed lines in Figure 7, where we plot the trends of both [N II]/[O II] and [N II]/Hα with R_{23}. Only when both these criteria were simultaneously satisfied we assigned the objects to the appropriate branch. However, there is a large number of 22 objects in our sample whose branches could not be firmly established, or remain dubious or contradictory, based on these criteria. These objects are represented by black filled circles connected by dotted lines in Figure 8, where we show how the M91-derived abundances change as a function of R_{23} parameter (top panel) and galactocentric distance (bottom panel). As the bottom panel of this figure shows dramatically, the R_{23} branch choice can yield very different conclusions about the radial trend of the oxygen abundance. This can make double-valued diagnostics like R_{23} inappropriate to study radial abundance gradients in galaxies, and as a minimum the results should be checked with additional diagnostics.

In summary, the ONS calibration gives the best agreement with the T_e method for the oxygen abundances of the M101 H II region sample among the strong-line diagnostics considered in our study. Most of the remaining empirically-calibrated strong-line methods diverge from the T_e method at low metallicities. The theoretically-calibrated diagnostics tend to systematically overestimate the abundances, compared to the T_e method. The excellent agreement of the ONS method with the T_e method is not too surprising, given that it was specifically calibrated using H II regions with well-measured T_e-based abundances (but so where the others). To further test its agreement with the T_e method we applied the ONS method to the H II region sample in the galaxy NGC 300 presented by Bresolin et al. (2009a), who found good agreement between the nebular abundances derived with the T_e method and the metallicities of blue supergiant stars (Kudritzki et al. 2008). The abundance gradient from the ONS method is found to be represented by the following linear fit: 12 + log(O/H) = 8.49(±0.02) − 0.33(±0.04) R/R_0. This agrees well with the fit obtained from the T_e method, 12 + log(O/H) = 8.57(±0.02) − 0.41(±0.03) R/R_0, and from the blue supergiants, 12 + log(O/H) = 8.59(±0.05) − 0.43(±0.06) R/R_0.

3.2.2. Abundance Variations Based on the ONS Diagnostic

In order to expand our analysis of possible spatial variations of the chemical abundances presented in Section 3.1, we used the oxygen abundances derived from the ONS method, which shows the best agreement with the T_e method for the enlarged sample of H II regions. However, adopting other strong-line diagnostics would yield the same conclusions concerning azimuthal variations in the inner disk.

The radial oxygen abundance gradient thus derived is shown in Figure 9. The solid line represents the least-square fit to the data.

We note that there are five objects at $R/R_0 = 0.81$ displaying a large abundance scatter. These are five individual emission knots located within the supergiant H II region NGC 5471 (see KG96). At least two of them have been associated with SNRs or the presence of high-velocity gas (Skillman 1985; Chu & Kennicutt 1986; Kennicutt & Garnett 1996). Peculiar ionization conditions in these knots could in principle affect the chemical abundance determination (but we note that the T_e-based oxygen abundances do not appear to be affected, and are quite homogeneous between the different knots). Thus, the apparently large abundance scatter between these data points, as seen in Figure 9, is unlikely to result from a real oxygen abundance inhomogeneity in this region (an interpretation supported by the T_e-based O/H measurements; see KBG03 for a discussion of the N/O ratio), but rather from a breakdown of the ONS diagnostic in this nebular complex.

The linear fit to the radial abundance gradient is not significantly affected by the inclusion of the knots in NGC 5471. We obtain:

$$12 + \log(\mathrm{O/H})_{\mathrm{ONS}} = 8.74(\pm 0.03) - 0.82(\pm 0.05) R/R_0 \quad (5)$$

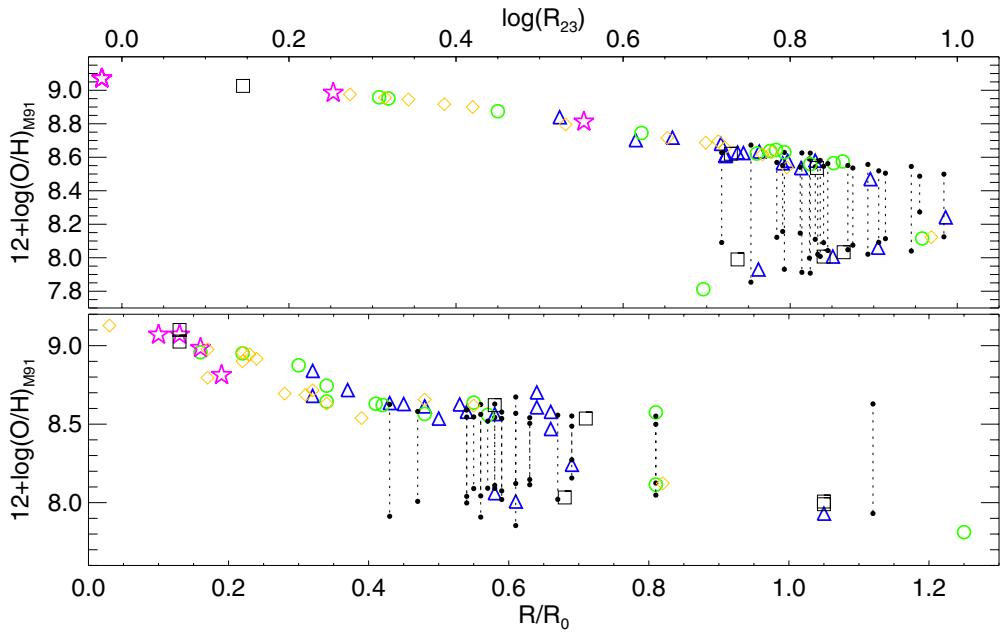

Figure 8. Top: oxygen abundances from R_{23} as a function of $\log(R_{23})$. Bottom: radial oxygen abundance distribution based on the M91 calibration of the R_{23} diagnostic. There are 22 objects (black filled circles) whose branches could not be univocally established and both upper and lower branch O/H values are shown as black dots connected with dot lines. Symbols as in Figure 1.

(A color version of this figure is available in the online journal.)

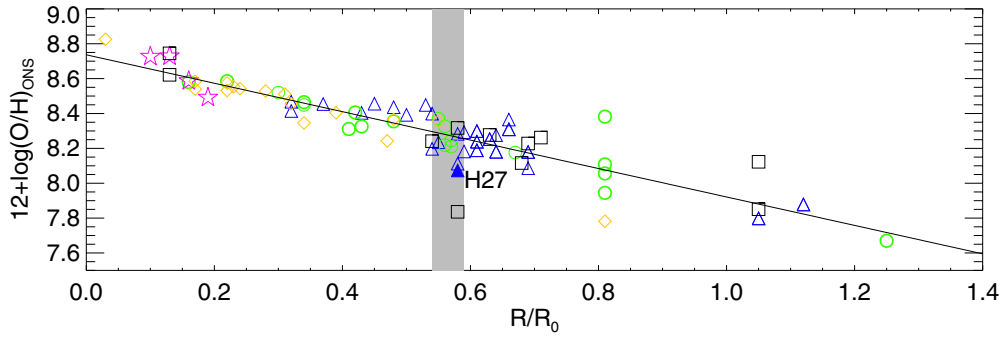

Figure 9. Radial oxygen abundance gradient from the ONS method. The solid line is the linear least-squares fit including 74 H II regions. H27 is marked by the filled triangle. The grey shadowed region is the same as in Figure 4. Symbols as in Figure 1.

(A color version of this figure is available in the online journal.)

with a linear Pearson correlation coefficient of −0.90. The intercept and the slope of the regression are consistent with the result derived from the direct method (Equation (3)).

As done earlier, in Figure 10 (top panel) we zoom into the radial range $R/R_0 = 0.54$ to 0.59 (highlighted in gray in Figure 9), and plot the oxygen abundance as a function of position angle (bottom panel). H II regions H27 (filled blue triangle) and H128 (filled green circle), which were found to be possible outliers from the radial abundance gradient obtained from the direct method, are not so using the ONS method. However, a new object, corresponding to slit 6 in van Zee et al. (1998), is now found to have quite a low O/H abundance ratio, $12 + \log(O/H) = 7.84$. This can be explained by the fact that the criterion used in the ONS method to assign an H II region to a particular excitation class fails for this particular nebula. The criterion, based on the [N II]/[S II] line ratio, assigns this object to the "hot" class, but if we calculate its O/H abundance as if it were a "warm" H II region its O/H ratio would increase by 0.3 dex, which would thus remove the systematic abundance offset relative to the other nebulae with similar galactocentric radius. The problem of misclassification in the ONS method has already been discussed by Bresolin et al. (2012). In addition, for the specific case of M101 Pilyugin et al. (2010) recommended to use the "hot" classification only for objects lying at $R/R_0 > 0.90$.

The rms scatter around the least-square fit for 74 H II regions (the enlarged sample with the five knots in NGC 5471 removed) is 0.10 dex. For the 17 objects in the grey shadowed region of Figure 9 the scatter is 0.14 dex, and for all the remaining objects it is 0.09 dex. However, if we focus on the 13 objects along arc A *only* we find that the scatter is comparable to what we find for the remaining objects (∼0.10 dex). In other words, based on the ONS method, we find no evidence for local inhomogeneities of the oxygen abundance along arc A.

4. A GLOBAL ASYMMETRY IN THE OXYGEN ABUNDANCE?

It is interesting to test not only for local chemical inhomogeneities, as done in the previous sections, but also for

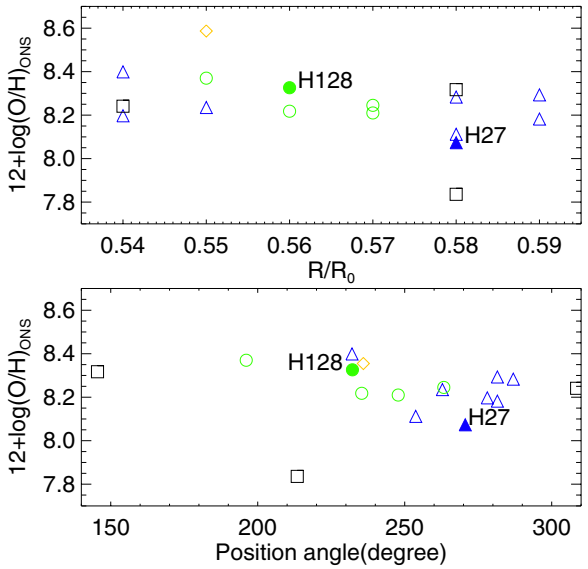

Figure 10. Detailed view of the shadowed region in Figure 9. The upper panel shows the relation between oxygen abundance and galactocentric distance in the range $R/R_0 = 0.54$ to 0.59. The bottom panel is the relation of oxygen abundance with position angle. The filled circle and triangle represent H128 and H27, respectively. Symbols as in Figure 1.

(A color version of this figure is available in the online journal.)

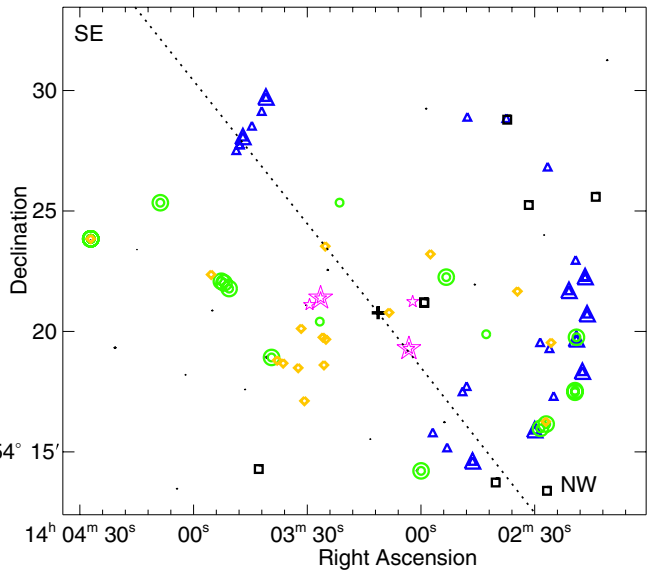

Figure 11. Spatial distribution of the H II regions in our sample in the plane of the sky. Our sample is geometrically divided into the "SE" (with position angle relative to the galaxy center between 37 and 217 deg) and "NW" part (complementary values of position angle). Symbols as in Figure 1.

(A color version of this figure is available in the online journal.)

large-scale azimuthal variations in the disk of M101. Is it true that the metal abundance distribution in the disk is azimuthally axisymmetric, as usually assumed in chemical evolution models? To start to answer this question in the case of M101, further examination of the two dimensional distribution of the oxygen abundance is required.

As a simple test, we divided the galaxy into two halves with respect to the major axis: an SE part (position angle: 37 to 217 deg, including 37 objects) and a NW part (complementary position angles, with 42 objects), as shown in Figure 11. KG96 suggested that objects in the SE have lower oxygen abundances

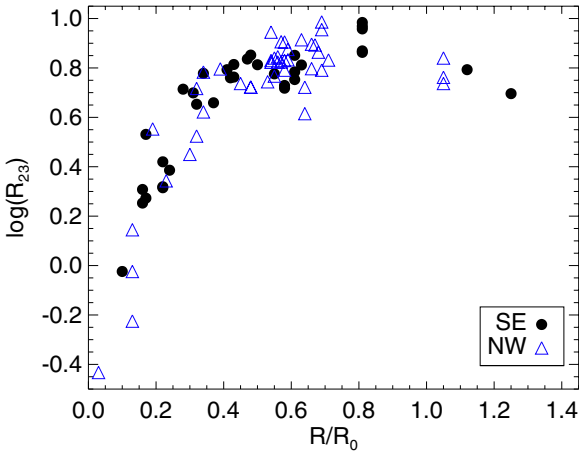

Figure 12. Radial dependence of the abundance parameter R_{23}. Filled circles—H II regions in the SE; open triangles—H II regions in the NW.

(A color version of this figure is available in the online journal.)

compared to H II region in the NW. This result was obtained from the use of the R_{23} parameter. We plotted the radial dependence of R_{23} in M101 in Figure 12 in the same way KG96 did, but including about twice the number of objects (79 versus 37). The distribution of data points is virtually the same for the two subsamples, and thus we do not confirm the non-axisymmetric distribution suggested by KG96 considering the R_{23} diagnostic alone.

As a further test, we used six different strong-line methods to calculate the oxygen abundances and fitted the radial distribution with linear functions of the form $12 + \log(\mathrm{O/H}) = a + b\times(R/R_0)$. Since we find (see Figure 13) that different abundance diagnostics yield qualitatively different radial trends in the outer disk, only object with $R/R_0 < 0.8$ were included in the fit. In Table 5 we summarize, for each diagnostic, the linear fit parameters a and b and their uncertainties, the Pearson correlation coefficients, the rms scatter of the fit, and the characteristic oxygen abundances measured at $R = 0.4\ R_0$, which correlate with the integrated galaxy metallicity (Zaritsky et al. 1994; Moustakas & Kennicutt 2006). Figure 13 illustrates the results of the fitting procedure for the two H II region subsamples (SE and NW) for each diagnostic. Table 5 shows that the linear radial gradient parameters (e.g., slope and zero point) are highly dependent on the abundance diagnostic adopted, which is not surprising given the different behaviors found among the strong-line methods when comparing with the T_e method. The possible breakdown of many of the diagnostics at low metallicities is evident in Figure 13, which shows that in several cases (e.g., for P01 and KD02-combine) the radial abundance gradient reaches a minimum abundance at $\sim$0.8 R_0, and then rises again in the outer disk. This situation has been more thoroughly discussed by Pilyugin (2003). If we believe that these results are unphysical, i.e., that the actual galactic gradient does not "turn over" at a certain galactocentric distance, we need to discard the abundances inferred from the strong-line diagnostics that are affected by this issue (we stress that the direct abundance are not affected). However, we point out that in recent years several reports of metallicity gradients becoming flat or turning over at large galactocentric radii in the Milky Way and other galaxies have been made (e.g., Worthey et al. 2005; Yong et al. 2012; Bresolin et al. 2009b). The radius where such a break appears to occur in M101 agrees well with the results from the recent work of Scarano & Lépine (2013), who noted a good correlation

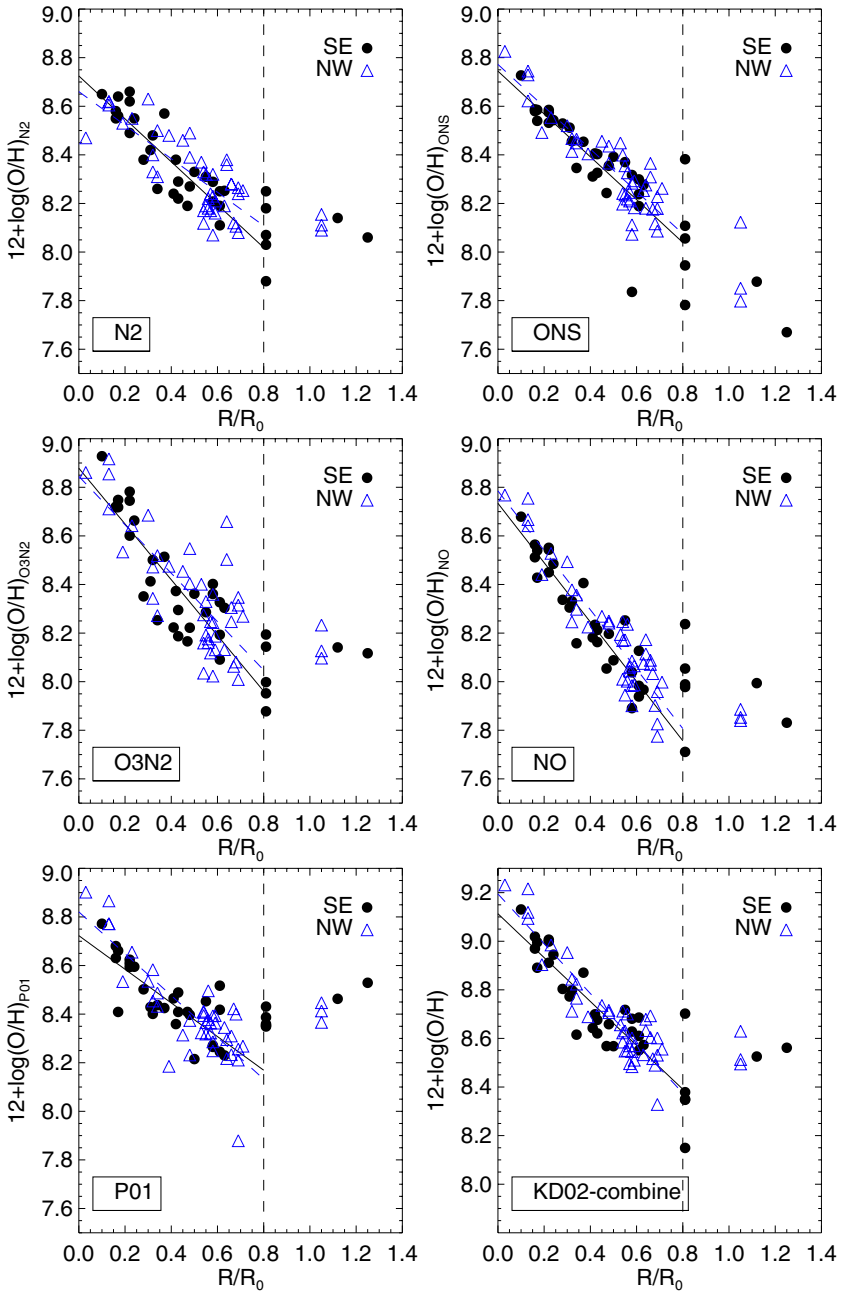

Figure 13. Radial oxygen abundance gradients in the SE and NW sections of M101 based on six different strong-line methods. The straight lines show the weighted linear regressions to the two samples, limited to data points located at $R < 0.8R_0$ (marked by the vertical dashed line).

(A color version of this figure is available in the online journal.)

between the radial positions of the break and corotation radii for a sample of spiral galaxies. Our Figure 13 shows, however, that the various abundance diagnostics we considered still leave some ambiguity concerning both the presence of the break and the gradient slope in the *outer disk* (this problem is absent in other outer disk nebular abundance studies, e.g., Bresolin et al. 2009b, 2012). Since the main goal of this work is to investigate the possibility of azimuthal variations in the *inner disk*, where the metallicity trends are less ambiguous, we decided to limit our analysis to $R/R_0 < 0.8$.

Doing so, the differences in slope and intercept of the linear regression between the SE and the NW portions of the disk are found to be smaller than the corresponding uncertainties, confirming the absence of obvious large-scale abundance variations in the azimuthal direction. A much more extensive spectroscopic coverage of M101 would be required to test for the presence of azimuthal variations among smaller sections (e.g., quadrants) of the disk.

5. SUMMARY AND CONCLUSIONS

Using a data sample of 79 H II regions, with 28 from our new observations (yielding 10 new detections of the [O III] λ4363 line) and the rest from additional sources in the literature, we have obtained and analyzed the radial oxygen abundance gradient in M101 based on the direct method ([O III] λ4363-based) as

Table 5
Parameters of the Separate Linear Fits to the Radial Gradients

Region	a	b	$\sigma(a)$	$\sigma(b)$	Correlation Coeff.	Scatter (rms)	$12 + \log(O/H)_{R=0.4R_0}$
PP04-N2							
ALL	8.68	−0.75	0.03	0.06	−0.83	0.10	8.38
SE	8.72	−0.88	0.04	0.10	−0.87	0.08	8.37
NW	8.66	−0.69	0.04	0.09	−0.79	0.10	8.38
PP04-O3N2							
ALL	8.85	−1.03	0.05	0.09	−0.80	0.14	8.44
SE	8.88	−1.15	0.06	0.15	−0.84	0.13	8.42
NW	8.84	−1.00	0.07	0.13	−0.77	0.15	8.45
P01							
ALL	8.77	−0.78	0.03	0.07	−0.81	0.10	8.46
SE	8.72	−0.69	0.04	0.10	−0.79	0.09	8.45
NW	8.82	−0.86	0.05	0.09	−0.82	0.11	8.48
ONS							
ALL	8.75	−0.85	0.03	0.06	−0.87	0.09	8.41
SE	8.74	−0.88	0.05	0.11	−0.84	0.10	8.39
NW	8.77	−0.87	0.04	0.07	−0.89	0.09	8.42
NO							
ALL	8.75	−1.18	0.03	0.06	−0.92	0.09	8.27
SE	8.73	−1.22	0.04	0.10	−0.93	0.08	8.25
NW	8.78	−1.22	0.04	0.08	−0.93	0.09	8.30
KD02-combine							
ALL	9.15	−0.96	0.03	0.06	−0.90	0.08	8.77
SE	9.11	−0.90	0.04	0.10	−0.88	0.08	8.75
NW	9.19	−1.02	0.04	0.07	−0.92	0.08	8.78

Note. Linear fits $a + b\times(R/R_0)$ including only objects with $R/R_0 \leqslant 0.8$.

well as various strong-line diagnostics. We found an exponential abundance profile with a gradient of -0.87 ± 0.04 dex ${R_0}^{-1}$ and a central abundance of $12 + \log(O/H) = 8.73 \pm 0.03$ from the direct oxygen abundance measurements. The scatter in the radial abundance gradient along arc A, located in the western disk of M101, is 0.15 ± 0.03 dex, while for the remaining H II regions of the M101 disk the scatter is 0.08 ± 0.01 dex. In the same section of the galaxy we found that one H II region, H27, deviates from the overall galactic abundance gradient, having a significantly lower oxygen abundance, $12 + \log(O/H)_{Te} = 7.96 \pm 0.08$, compared to nearby objects. One additional neighboring nebula, H128, has instead a large metallicity value, $12 + \log(O/H)_{Te} = 8.45 \pm 0.04$, for its galactocentric distance, as already found by Kennicutt et al. (2003). These results provide evidence that marginally significant deviations from local metallicity homogeneity can arise in the interstellar medium of this part of the galaxy over spatial scales of a few kpc.

Among the strong-line abundance diagnostics we considered to derive the O/H abundance ratio for the full sample of 79 H II regions we found that the ONS method (Pilyugin et al. 2010) provides the best agreement with the direct method. With the ONS method we did not find any significant difference in the abundance scatter between H II regions in the western arc of M101 and the rest of the galaxy, being approximately 0.10 dex in both cases. The rather large deviations from the main abundance radial gradient measured for H27 and H128 from the direct method are not confirmed by the ONS method. On the other hand, the ONS method provides a large (0.4 dex) spread in the abundance of individual knots in the supergiant H II region NGC 5471, which is not seen in the T_e-based data, and which we interpret as an example of the fact that strong-line method results should always be taken with care and be considered valid in a "statistical" sense. For individual measurements the T_e method should be preferred. On the other hand, the result of our test of possible large-scale azimuthal abundance trends between two opposite sides of M101 using strong-line methods, i.e., that there is no detectable variation, should be considered robust. The small scatter we generally observe in the abundance gradient, when we consider that it includes H II regions on opposite sides of the galaxy, is also a good indication for a fairly homogeneous azimuthal abundance distribution.

In general, findings of large *local* deviations from abundance homogeneity obtained from strong-line methods should be verified with direct, T_e-based measurements. We point out that the abundances of individual emission knots within large (∼1 kpc) H II region complexes are consistent with chemical abundance homogeneity when using T_e-based data. Besides the case of NGC 5471 mentioned above, this is true for the NGC 5447 (H128, H143, H149) and NGC 5462 (H1159, H1170, H1176) complexes. On the other hand, claiming sizable inhomogeneities from abundances measured from some strong-line indicators appears risky. For example, the N2 parameter (in both the Pettini & Pagel 2004 and Pérez-Montero & Contini 2009 versions of the calibration considered here) yields abundance variations on the order of ∼0.2 dex between the few knots contained in the H II region complexes mentioned above, i.e., over spatial scales of a few hundred pc. Among the N-based diagnostics, the NO indicator calibrated by Bresolin (2007) appears much more robust, yielding variations on the order of 0.03 dex among these objects.

It is tempting to try and interpret the relatively small abundance peculiarity we detected in the western disk of M101 using the direct method with the notion that metallicity inhomogeneities could arise from metal-poor gas infall and galaxy

interactions. The presence of high-velocity clouds and distortions in the spiral structure in the eastern disk of M101 (van der Hulst & Sancisi 1988; Waller et al. 1997; Sancisi et al. 2008) can be attributed to tidal interactions between M101 and one or more of its surrounding neighboring dwarf galaxies. Very recently, Mihos et al. (2012) presented a new deep H I map of the M101 group, which revealed the presence of newly-discovered H I clouds and an H I "plume" extending from the SW of M101, likely of tidal nature. It is of course difficult to associate any of these features with the observed metallicity patterns in the M101 disk, but it is tantalizing to observe that the marginally larger scatter in the abundance distribution that we detect in the western arc is taking place on the same side of the galaxy where these tidal features appear now more evident. Future studies should address this possibility by obtaining a large number of high-quality spectroscopic observations and direct abundances in this part of M101.

Y.L. would like to thank J. Patrick Henry for statistical consult about the errors on the scatters, R. P. Kudritzki for useful comments, and T. -T. Yuan for her help with various scientific discussions. F.B. gratefully acknowledges partial support from the National Science Foundation grants AST-0707911 and AST-1008798. We thank the anonymous referee for constructive comments that helped us to improve the quality of the paper.

REFERENCES

Aller, L. H. (ed.) 1984, Physics of Thermal Gaseous Nebulae (Astrophysics and Space Science Library, Vol. 112; Dordrecht: Reidel)
Baldwin, J. A., Phillips, M. M., & Terlevich, R. 1981, PASP, 93, 5
Balser, D. S., Rood, R. T., Bania, T. M., & Anderson, L. D. 2011, ApJ, 738, 27
Bresolin, F. 2007, ApJ, 656, 186
Bresolin, F. 2011, ApJ, 729, 56
Bresolin, F., Gieren, W., Kudritzki, R., et al. 2009a, ApJ, 700, 309
Bresolin, F., Kennicutt, R. C., & Ryan-Weber, E. 2012, ApJ, 750, 122
Bresolin, F., Kennicutt, R. C., Jr., & Garnett, D. R. 1999, ApJ, 510, 104
Bresolin, F., Ryan-Weber, E., Kennicutt, R. C., & Goddard, Q. 2009b, ApJ, 695, 580
Cedrés, B., Cepa, J., Bongiovanni, Á., et al. 2012, A&A, 545, A43
Chiappini, C., Matteucci, F., & Romano, D. 2001, ApJ, 554, 1044
Chu, Y.-H., & Kennicutt, R. C., Jr. 1986, ApJ, 311, 85
de Blok, W. J. G., Walter, F., Brinks, E., et al. 2008, AJ, 136, 2648
de Vaucouleurs, G., de Vaucouleurs, A., Corwin, H. G., Jr., et al. 1991, Third Reference Catalogue of Bright Galaxies (Berlin: Springer)
Franchetti, N. A., Gruendl, R. A., Chu, Y.-H., et al. 2012, AJ, 143, 85
Freedman, W. L., Madore, B. F., Gibson, B. K., et al. 2001, ApJ, 553, 47
Fu, J., Hou, J. L., Yin, J., & Chang, R. X. 2009, ApJ, 696, 668
Garnett, D. R. 1992, AJ, 103, 1330
Hodge, P. W., Gurwell, M., Goldader, J. D., & Kennicutt, R. C., Jr. 1990, ApJS, 73, 661
Howarth, I. D. 1983, MNRAS, 203, 301
Kauffmann, G., Heckman, T. M., Tremonti, C., et al. 2003, MNRAS, 346, 1055
Kennicutt, R. C., Bresolin, F., & Garnett, D. R. 2003, ApJ, 591, 801
Kennicutt, R. C., & Garnett, D. R. 1996, ApJ, 456, 504
Kewley, L. J., & Dopita, M. A. 2002, ApJS, 142, 35
Kewley, L. J., Dopita, M. A., Sutherland, R. S., Heisler, C. A., & Trevena, J. 2001, ApJ, 556, 121
Kewley, L. J., & Ellison, S. L. 2008, ApJ, 681, 1183
Kobulnicky, H. A., Kennicutt, R. C., Jr., & Pizagno, J. L. 1999, ApJ, 514, 544
Kudritzki, R.-P., Urbaneja, M. A., Bresolin, F., et al. 2008, ApJ, 681, 269
Lépine, J. R. D., Cruz, P., Scarano, S., Jr., et al. 2011, MNRAS, 417, 698
Luck, R. E., Gieren, W. P., Andrievsky, S. M., et al. 2003, A&A, 401, 939
Lupton, R. 1993, Statistics in Theory and Practice (Princeton, NJ: Princeton Univ. Press)
McGaugh, S. S. 1991, ApJ, 380, 140
Mihos, C., Keating, K., Holley-Bockelmann, K., Pisano, D. J., & Kassim, N. 2012, ApJ, 761, 186
Moustakas, J., & Kennicutt, R. C., Jr. 2006, ApJ, 651, 155
Pagel, B. E. J., Edmunds, M. G., Blackwell, D. E., Chun, M. S., & Smith, G. 1979, MNRAS, 189, 95
Pedicelli, S., Bono, G., Lemasle, B., et al. 2009, A&A, 504, 81
Pérez-Montero, E., & Contini, T. 2009, MNRAS, 398, 949
Pérez-Montero, E., & Díaz, A. I. 2005, MNRAS, 361, 1063
Pettini, M., & Pagel, B. E. J. 2004, MNRAS, 348, L59
Pilyugin, L. S. 2001, A&A, 369, 594
Pilyugin, L. S. 2003, A&A, 399, 1003
Pilyugin, L. S. 2005, A&A, 436, L1
Pilyugin, L. S., Vílchez, J. M., & Thuan, T. X. 2010, ApJ, 720, 1738
Rosales-Ortega, F. F., Díaz, A. I., Kennicutt, R. C., & Sánchez, S. F. 2011, MNRAS, 415, 2439
Rosolowsky, E., & Simon, J. D. 2008, ApJ, 675, 1213
Roy, J.-R., & Kunth, D. 1995, A&A, 294, 432
Sancisi, R., Fraternali, F., Oosterloo, T., & van der Hulst, T. 2008, A&ARv, 15, 189
Sanders, N. E., Caldwell, N., McDowell, J., & Harding, P. 2012, ApJ, 758, 133
Scarano, S., & Lépine, J. R. D. 2013, MNRAS, 428, 625
Scarano, S., Jr., Lépine, J. R. D., & Marcon-Uchida, M. M. 2011, MNRAS, 412, 1741
Searle, L. 1971, ApJ, 168, 327
Seaton, M. J. 1979, MNRAS, 187, 73P
Shaw, R. A., & Dufour, R. J. 1995, PASP, 107, 896
Skillman, E. D. 1985, ApJ, 290, 449
Smith, H. E. 1975, ApJ, 199, 591
Stasińska, G. 2005, A&A, 434, 507
Storey, P. J., & Hummer, D. G. 1995, MNRAS, 272, 41
Storey, P. J., & Zeippen, C. J. 2000, MNRAS, 312, 813
Twarog, B. A., Ashman, K. M., & Anthony-Twarog, B. J. 1997, AJ, 114, 2556
van der Hulst, T., & Sancisi, R. 1988, AJ, 95, 1354
van Zee, L., Salzer, J. J., Haynes, M. P., O'Donoghue, A. A., & Balonek, T. J. 1998, AJ, 116, 2805
Vila-Costas, M. B., & Edmunds, M. G. 1992, MNRAS, 259, 121
Waller, W. H., Bohlin, R. C., Cornett, R. H., et al. 1997, ApJ, 481, 169
Worthey, G., España, A., MacArthur, L. A., & Courteau, S. 2005, ApJ, 631, 820
Yang, C.-C., & Krumholz, M. 2012, ApJ, 758, 48
Yin, S. Y., Liang, Y. C., Hammer, F., et al. 2007, A&A, 462, 535
Yong, D., Carney, B. W., & Friel, E. D. 2012, AJ, 144, 95
Zaritsky, D., Kennicutt, R. C., Jr., & Huchra, J. P. 1994, ApJ, 420, 87
Zurita, A., & Bresolin, F. 2012, MNRAS, 427, 1463